Exact solutions for pure torsion of shape memory alloy circular bars

Reza Mirzaeifar, Reginald DesRoches, Arash Yavari *

School of Civil and Environmental Engineering, Georgia Institute of Technology, Atlanta, GA 30332, USA

ARTICLE INFO

ABSTRACT

Shape memory alloy (SMA) structures are usually analyzed numerically; there are very few closed-form solutions in the literature. In this paper, we study the pure torsion of SMA bars with circular cross sections. First, a three-dimensional phenomenological macroscopic constitutive model for polycrystalline SMAs is reduced to the one-dimensional pure shear case and then a closed-form solution for torsional response of SMA bars in loading and unloading is obtained. Several case studies are presented in order to investigate the influence of different parameters, e.g. temperature and material properties on the torsional response of SMA circular bars.

© 2010 Elsevier Ltd. All rights reserved.

1. Introduction

Along with the recent increase in the use of shape memory alloy (SMA) devices in a wide variety of applications, various numerical methods have been developed for analyzing these devices (Qidwai and Lagoudas, 2000; Liew et al., 2002; Mahapatra and Melnik, 2007). Due to the complexity of the nonlinear numerical algorithms that are currently used for modeling shape memory alloys, there are numerous parameters that can affect the accuracy of these methods in analyzing even a simple SMA structure. The necessity of validating the outputs of numerical simulations along with the difficulty of performing experimental tests on SMAs, is the main motivation for seeking analytical or semi-analytical solutions for some SMA devices (Mirzaeifar, 2009).

Recent studies have shown that SMAs can be efficiently used in improving the response of structures, e.g. buildings and bridges subjected to earthquake loads (DesRoches and Smith, 2004; Andrawes and DesRoches, 2007, 2008). The unique ability of SMAs in recovering large scale strains (pseudoelasticity) makes them a desirable option for en-

ergy dissipating devices in multiple-frame structures like bridges. Recently, Speicher et al. (2009) introduced a new device with shape memory alloy helical springs that can be used as bracing elements in buildings. SMA helical springs were subjected to cyclic loads and it was shown that Nitinol helical springs are efficient devices for recentering and damping in a vast range of structures besides their ability in minimizing the residual deformations in structures after an earthquake. In addition of being potential energy dissipating devices, SMA helical springs have a vast range of industrial applications as active actuators (Dong et al., 2008; Leea et al., 2009).

The simplest method for analyzing helical springs is to assume that each portion of a spring acts as a straight bar under torsion. It can be shown that when the spring index (the ratio of mean coil radius to the cross section radius) is large and the helix angle is small, this assumption leads to fairly accurate results (Wahl, 1944). In a series of studies Ancker and Goodier (1958a,b,c) investigated the accuracy of this assumption in some detail and modified it to obtain a more accurate solution for helical springs considering the curvature effects. In one of the first studies on SMA helical springs, Tobushi and Tanaka (1991) considered the pure torsion assumption for analyzing a helical spring under axial load. They used Tanaka's constitutive model (Tanaka, 1986) but in the stress–strain relation the hardening during phase transformation is ignored and the material is treated as

* Corresponding author. Address: School of Civil and Environmental Engineering, Georgia Institute of Technology, 790 Atlantic Dr., Atlanta, GA 30332, USA. Fax: +1 404 894 2278.
E-mail address: arash.yavari@ce.gatech.edu (A. Yavari).

perfectly plastic. Although this assumption simplifies the solution remarkably, experimental results show that the hardening response in stress–strain relations for polycrystalline SMAs can not be ignored. In another effort for analyzing SMA helical springs, Toi et al. (2004) modified the Brinson's one-dimensional constitutive model (Brinson, 1993) for SMAs and implemented it in an incremental finite element formulation using Timoshenko beam elements. In their study, helical SMA springs are modeled numerically and simulation outputs are compared with experimental results.

In the present study, pure torsion of SMA bars with circular cross sections is considered. This is the first step in analysis of SMA helical springs with large spring index and small helix angle. We should mention that torsion of SMA bars have been studied by several researchers in recent years. Lim and McDowell (1999) reported the behavior of SMA thin-walled tubes subjected to axial–torsional proportional and nonproportional loading by conducting several experiments. Chung et al. (2006) presented a numerical simulation for pseudoelastic behavior of shape memory alloy circular rods under tension/torsion combined loadings. Brinson's phase transformation formulation and an analogy with traditional plasticity were used.

Clearly pure torsion is an important benchmark problem that can be used in validating various numerical simulations of SMAs. Pure torsion is also important as a first step in analysis of SMA springs. A general three-dimensional constitutive relation for shape memory alloys is first reduced to an appropriate one-dimensional form suitable for implementation in pure torsion. An explicit expression is derived for shear stress as a function of geometric specifications, material constants, and shear strain. Response of circular bars in torsion is carefully analyzed by considering different possibilities that may happen for various loading levels and some case studies are presented for investigating the effect of material properties and temperature on the behavior of circular bars in loading and unloading conditions.

This paper is organized as follows. In Section 2 a general three-dimensional constitutive equation for polycrystalline SMAs is briefly reviewed. The three-dimensional constitutive relations are reduced to a one-dimensional constitutive equation for pure torsion in Section 3 and an explicit relation is derived for shear stress. Different case studies are presented in Section 4. Torsion of an SMA thin-walled tube is considered with the purpose of validating an incremental based finite element simulation. Several case studies are presented. SMA solid bars with circular cross sections subjected to torsion and different parameters like temperature and material properties are studied in both loading and unloading cases. Conclusions are given in Section 5.

2. General constitutive model

We use Boyd and Lagoudas (1996) and Qidwai and Lagoudas (2000)'s three-dimensional phenomenological macroscopic constitutive model for polycrystalline SMAs. In this constitutive model one starts with the following expression for the total Gibbs free energy G:

$$G(\boldsymbol{\sigma}, T, \boldsymbol{\epsilon}^t, \xi) = -\frac{1}{2\rho}\boldsymbol{\sigma} : \mathbb{S} : \boldsymbol{\sigma} - \frac{1}{\rho}\boldsymbol{\sigma} : \left[\boldsymbol{\alpha}(T - T_0) + \boldsymbol{\epsilon}^t\right]$$
$$+ c\left[(T - T_0) - T\ln\left(\frac{T}{T_0}\right)\right] - s_0 T + u_0$$
$$+ \frac{1}{\rho}f(\xi), \tag{1}$$

where $\mathbb{S}$, $\boldsymbol{\alpha}$, c, ρ, s_0 and u_0 are the effective compliance tensor, effective thermal expansion coefficient tensor, effective specific heat, mass density, effective specific entropy, and effective specific internal energy at the reference state, respectively. The symbols $\boldsymbol{\sigma}$, T, T_0, $\boldsymbol{\epsilon}^t$ and ξ represent the Cauchy stress tensor, temperature, reference temperature, transformation strain and martensitic volume fraction, respectively. All the effective material properties are assumed to vary with the martensitic volume fraction (ξ) as follows:

$$\mathbb{S} = \mathbb{S}^A + \xi\Delta\mathbb{S}, \quad \boldsymbol{\alpha} = \boldsymbol{\alpha}^A + \xi\Delta\boldsymbol{\alpha}, \quad c = c^A + \xi\Delta c,$$
$$s_0 = s_0^A + \xi\Delta s, \quad u_0 = u_0^A + \xi\Delta u_0, \tag{2}$$

where the superscripts A and M represent the austenite and martensite phases, respectively. The symbol $\Delta(\cdot)$ denotes the difference of a quality $(\cdot)$ between the martensitic and austenitic phases, i.e. $\Delta(\cdot) = (\cdot)^M - (\cdot)^A$. In (1), $f(\xi)$ is a hardening function that models the transformation strain hardening in the SMA material. In the Boyd–Lagoudas' polynomial hardening model, this function is given by

$$f(\xi) = \begin{cases} \frac{1}{2}\rho b^M \xi^2 + (\mu_1 + \mu_2)\xi, & \dot{\xi} > 0, \\ \frac{1}{2}\rho b^A \xi^2 + (\mu_1 - \mu_2)\xi, & \dot{\xi} < 0, \end{cases} \tag{3}$$

where ρb^A, ρb^M, μ_1 and μ_2 are material constants for transformation strain hardening. The first condition in (3) represents the forward phase transformation $(A \rightarrow M)$ and the second condition represents the reverse phase transformation $(M \rightarrow A)$. The constitutive relation of a shape memory material can be obtained by using the total Gibbs free energy as

$$\boldsymbol{\epsilon} = -\rho\frac{\partial G}{\partial\boldsymbol{\sigma}} = \mathbb{S} : \boldsymbol{\sigma} + \boldsymbol{\alpha}(T - T_0) + \boldsymbol{\epsilon}^t. \tag{4}$$

Considering the fact that any change in the state of the system is only possible by a change in the internal state variable ξ (Bo and Lagoudas, 1999), the evolution of the transformation strain tensor is related to the evolution of the martensitic volume fraction as

$$\dot{\boldsymbol{\epsilon}}^t = \boldsymbol{\Gamma}\dot{\xi}, \tag{5}$$

where $\boldsymbol{\Gamma}$ represents a transformation tensor related to the deviatoric stress tensor and determines the flow direction as

$$\boldsymbol{\Gamma} = \begin{cases} \frac{3}{2}\frac{H}{\bar{\sigma}}\boldsymbol{\sigma}', & \dot{\xi} > 0, \\ \frac{H}{\bar{\epsilon}^{tr}}\boldsymbol{\epsilon}^{tr}, & \dot{\xi} < 0. \end{cases} \tag{6}$$

In (6), H is the maximum uniaxial transformation strain and $\boldsymbol{\epsilon}^{tr}$ represents the transformation strain at the reverse phase transformation. The terms $\boldsymbol{\sigma}'$, $\bar{\sigma}$ and $\bar{\epsilon}^{tr}$ are the deviatoric stress tensor, the second deviatoric stress invariant and the second deviatoric transformation strain invariant, respectively, and are expressed as

$$\boldsymbol{\sigma}' = \boldsymbol{\sigma} - \frac{1}{3}(\mathrm{tr}\boldsymbol{\sigma})\mathbf{I}, \quad \bar{\sigma} = \sqrt{\frac{3}{2}\boldsymbol{\sigma}' : \boldsymbol{\sigma}'},$$

$$\bar{\epsilon}^{tr} = \sqrt{\frac{2}{3}\boldsymbol{\epsilon}^{tr} : \boldsymbol{\epsilon}^{tr}}, \tag{7}$$

where $\mathbf{I}$ is the identity tensor.

An additional constraint on the material behavior is obtained by using the Second Law of Thermodynamics in the form of non-negativeness of the rate of entropy production density (Qidwai and Lagoudas, 2000):

$$\boldsymbol{\sigma} : \dot{\boldsymbol{\epsilon}}^t - \rho\frac{\partial G}{\partial \xi}\dot{\xi} = \pi\dot{\xi} \geqslant 0, \tag{8}$$

where π is a thermodynamic force and can be obtained by substituting (1) and (5) into (8) as

$$\pi = \boldsymbol{\sigma} : \boldsymbol{\Gamma} + \frac{1}{2}\boldsymbol{\sigma} : \Delta\mathbb{S} : \boldsymbol{\sigma} + \Delta\boldsymbol{\alpha} : \boldsymbol{\sigma}(T - T_0)$$
$$- \rho\Delta c\left[(T - T_0) - T\ln\left(\frac{T}{T_0}\right)\right] + \rho\Delta s_0 T$$
$$- \frac{\partial f}{\partial \xi} - \rho\Delta u_0. \tag{9}$$

Now, the transformation function that controls the onset of direct and reverse phase transformation is defined as

$$\Phi = \begin{cases} \pi - Y, & \dot{\xi} > 0, \\ -\pi - Y, & \dot{\xi} < 0, \end{cases} \tag{10}$$

wheres Y is a measure of internal dissipation due to microstructural changes during phase transformation. The transformation function represents the elastic domain in the stress–temperature state. In other words, when $\Phi < 0$ the material response is elastic and the martensitic volume fraction does not change ($\dot{\xi} = 0$). During the forward phase transformation from austenite to martensite ($\dot{\xi} > 0$) and the reverse phase transformation from martensite to austenite ($\dot{\xi} < 0$), the state of stress, temperature and martensitic volume fraction should remain on the transformation surface, which is characterized by $\Phi = 0$. It can be seen that transformation surface in the stress–temperature space is represented by two separate faces that are defined by $\xi = 0$ and $\xi = 1$. Any state of stress–temperature inside the inner surface ($\xi = 0$) represents the austenite state with an elastic response. Outside the surface $\xi = 1$, the material is fully martensite and behaves elastically. For any state of stress–temperature on or in between these two surfaces the material behavior is inelastic and a forward transformation occurs. A similar transformation surface exists for the reverse phase transformation.

3. Reduction of the constitutive equations for pure torsion

Analysis of solid members with a uniform cross section of general shape in torsion is a classical problem in elasticity and is commonly referred to as the Saint–Venant's problem after the French mathematician Barré de Saint–Venant. In 1784, Coulomb presented a solution for prismatic bars with circular cross sections in torsion. For many years, this formulation was used for torsional analysis of bars with arbitrary cross sections. Later it was shown that the Coulomb's formulation, which ignores the cross section warpage[1] is not valid, in general. There were many unsuccessful attempts for formulating the torsion of a bar with a general cross section consistent with elasticity equations (for a historical review see Higgins, 1942). Finally, In 1874, Saint–Venant published the correct formulation of the torsion problem in a series of three papers (Higgins, 1942). Based on the general solution of Saint–Venant, it can be shown that the no warpage assumption is valid for bars with circular cross section (Sokolnikoff, 1956) and some other special cross sections (Chen, 2004). According to Saint–Venant's solution the state of stress and strain is one-dimensional and shear strain varies linearly from the central axis toward the outer radius.[2]

In the case of circular bars, the general three-dimensional constitutive relations introduced in the previous section can be reduced to a one-dimensional constitutive equation. The stress, strain, and transformation strain tensors have the following forms:

$$\boldsymbol{\sigma} = \begin{bmatrix} 0 & 0 & 0 \\ 0 & 0 & \tau_{\theta z} \\ 0 & \tau_{\theta z} & 0 \end{bmatrix}, \quad \boldsymbol{\epsilon} = \begin{bmatrix} 0 & 0 & 0 \\ 0 & 0 & \epsilon_{\theta z} \\ 0 & \epsilon_{\theta z} & 0 \end{bmatrix},$$

$$\boldsymbol{\epsilon}^t = \begin{bmatrix} 0 & 0 & 0 \\ 0 & 0 & \epsilon_{\theta z}^t \\ 0 & \epsilon_{\theta z}^t & 0 \end{bmatrix}, \tag{11}$$

where $\tau_{\theta z}$, $\epsilon_{\theta z}$ and $\epsilon_{\theta z}^t$ are the shear stress, shear strain and transformation shear strains, respectively. Using $\mathrm{tr}\boldsymbol{\sigma} = 0$ in (7) the deviatoric stress tensor will be the same as the stress tensor, $\boldsymbol{\sigma}' = \boldsymbol{\sigma}$. The second deviatoric stress and transformation strain invariants are reduced to read:

$$\bar{\sigma} = \sqrt{3}|\tau_{\theta z}|, \quad \bar{\epsilon}^{tr} = \frac{2}{\sqrt{3}}|\epsilon_{\theta z}^{tr}|. \tag{12}$$

The transformation tensor for the pure torsion is expressed as:

$$\boldsymbol{\Gamma}^+ = \frac{\sqrt{3}}{2}H\,\mathrm{sgn}(\tau_{\theta z})\begin{bmatrix} 0 & 0 & 0 \\ 0 & 0 & 1 \\ 0 & 1 & 0 \end{bmatrix},$$

$$\boldsymbol{\Gamma}^- = \frac{\sqrt{3}}{2}H\,\mathrm{sgn}(\epsilon_{\theta z}^{tr})\begin{bmatrix} 0 & 0 & 0 \\ 0 & 0 & 1 \\ 0 & 1 & 0 \end{bmatrix}, \tag{13}$$

where $\mathrm{sgn}(\cdot)$ is the sign function and the superscripts + and − for $\boldsymbol{\Gamma}$ represent the forward and inverse phase transformations, respectively. Substituting (13) into (9) and (10) and using the following relation between the constitutive model parameters:

---

[1] In a cross section with warpage, the planar cross sections perpendicular to the axis of the bar before deformation will not remain planar after deformation.

[2] Considering a cross section in the xy-plane (z is along the bar axis), the state of shear strain at a point in the cross section is $\gamma_{zx} = 2\epsilon_{zx} = \theta\left(\frac{\partial\psi}{\partial x} - y\right)$ and $\gamma_{zy} = 2\epsilon_{zy} = \theta\left(\frac{\partial\psi}{\partial y} + x\right)$, where θ is the twist angle per unit length and ψ represents the warping function that represents the cross section deformation along the z-axis. Clearly, zero warpage leads to the linear distribution of shear strains through the thickness (Sokolnikoff, 1956).

$$\rho\Delta u_0 + \mu_1 = \frac{1}{2}\rho\Delta s_0(M_s + A_f), \rho b^A = -\rho\Delta s_0(A_f - A_s),$$

$$\rho b^M = -\rho\Delta s_0(M_s - M_f), Y = -\frac{1}{2}\rho\Delta s_0(A_f - M_s) - \mu_2,$$

$$\mu_2 = \frac{1}{4}(\rho b^A - \rho b^M),$$

(14)

explicit expressions for the martensitic volume fraction in direct and inverse phase transformation are obtained as

$$\xi^+ = \frac{1}{\rho b^M}\left\{\sqrt{3}H|\tau_{\theta z}| + 2\tau_{\theta z}^2\Delta S_{44} + f^+(T)\right\},$$

(15)

$$\xi^- = \frac{1}{\rho b^A}\left\{\sqrt{3}H\tau_{\theta z}\text{sgn}(\epsilon_{\theta z}^{tr}) + 2\tau_{\theta z}^2\Delta S_{44} + f^-(T)\right\},$$

(16)

where

$$f^+(T) = \rho\Delta c\left[(T - T_0) - T\ln\left(\frac{T}{T_0}\right)\right] + \rho\Delta s_0(T - M_s),$$

(17)

$$f^-(T) = \rho\Delta c\left[(T - T_0) - T\ln\left(\frac{T}{T_0}\right)\right] + \rho\Delta s_0(T - A_f).$$

(18)

The parameters M_s and A_f are the martensitic start and austenite finish temperatures, respectively. By substituting the explicit expression of the martensitic volume fraction in (5) and after integrating from zero to an arbitrary time, the transformation shear strain can be calculated. The constitutive relation (4) is now reduced to read:

$$\epsilon_{\theta z} = \frac{1+v}{E_A + \xi^\pm(E_M - E_A)}\tau_{\theta z}$$
$$+ \frac{1}{\rho b^\pm}\left\{\frac{3}{2}H^2\tau_{\theta z} + \sqrt{3}H\tau_{\theta z}^2\aleph^\pm\Delta S_{44} + \frac{\sqrt{3}}{2}H\aleph^\pm f^\pm(T)\right\},$$

(19)

where v is Poisson's ratio that is assumed to be the same for both phases. The + and − symbols are used for the direct and reverse phase transformations, respectively, and the other parameters are: $\aleph^+ = \text{sgn}(\tau_{\theta z})$, $\aleph^- = \text{sgn}(\epsilon_{\theta z}^{tr})$, $\rho b^+ = \rho b^M$ and $\rho b^- = \rho b^A$. For a bar with a circular cross section, the shear strain in (19) can be related to twist angle per unit length as $\epsilon_{\theta z} = \frac{1}{2}r\theta$, where r is the distance from the axis of the bar. Substituting (15) into (19) and considering the special case in which both the shear stress and the shear transformation strains are positive (19) can be rewritten as:

$$\tau_{\theta z}^4 + F_1\tau_{\theta z}^3 + (F_2 + F_2^*r\theta)\tau_{\theta z}^2 + (F_3 + F_3^*r\theta)\tau_{\theta z}$$
$$+ (F_4 + F_4^*r\theta) = 0,$$

(20)

where,

$$F_1 = -\frac{\sqrt{3}H}{\Delta S_{44}},$$

$$F_2 = \frac{1}{4}\frac{3\Delta EH^2 + 4\Delta E\Delta S_{44}f^\pm(T) + 2\rho b^\pm E_A\Delta S_{44}}{\Delta E\Delta S_{44}^2},$$

$$F_3 = \frac{\sqrt{3}}{12}\frac{6\Delta EH^2 f^\pm(T) + 3\rho b^\pm E_A H^2 + 2(1+v)(\rho b^\pm)^2}{H\Delta E\Delta S_{44}^2},$$

$$F_4 = \frac{1}{4}\frac{f^\pm(T)(\Delta Ef^\pm(T) + \rho b^\pm E_A)}{\Delta E\Delta S_{44}^2},$$

$$F_2^* = -\frac{1}{6}\frac{\rho b^\pm\sqrt{3}}{\Delta S_{44}H},$$

$$F_3^* = -\frac{1}{4}\frac{\rho b^\pm}{\Delta S_{44}^2},$$

$$F_4^* = -\frac{\sqrt{3}}{12}\frac{\rho b^\pm(\Delta Ef^\pm(T) + \rho b^\pm E_A)}{H\Delta E\Delta S_{44}^2},$$

(21)

in which $\Delta E = (E_M - E_A)$. The relation (20) is a quartic equation that can be solved analytically using Ferrari's method[3] for finding the shear stress $\tau_{\theta z}$ as a function of twist angle in an arbitrary radius as:

$$\tau_{\theta z} = \wp^\pm(r, \theta),$$

(22)

which is given explicitly in Appendix A.

4. Torsion of a SMA bar with circular cross section

In this section, several case studies are presented for torsion of circular SMA bars. In these numerical examples, two different sets of material parameters are used as shown in Table 1. The first set of properties are some generic values given in Qidwai and Lagoudas (2000) and later used by many researchers in reporting numerical simulations of SMAs. The second set of parameters are based on an experimental work by Jacobus et al. (1996) on Ni$_{50}$Ti$_{50}$ alloy. The required material constants for the reduced constitutive model are extracted from the experimental data by Qidwai and Lagoudas (2000).

4.1. Thin-walled SMA tube

As the first case study, a thin-walled SMA tube with radius $R = 3$ mm and length $L = 4$ cm is considered. The tube is fixed at one end and the other end is twisted. The material properties (Material I) in Table 1 are used. The temperature is assumed to be $T = 315$ K. We compare the results of the present analytic solution with a finite element simulation. The details of implementing the reduced constitutive equation in a displacement based finite element formulation is given in Mirzaeifar et al. (2009). The three-dimensional constitutive relations of Section 2 are used and an appropriate user subroutine (UMAT) is written by FORTRAN in the commercially available finite element program ABAQUS that enables this code to model SMA structures using solid elements and some two-dimensional elements. The developed finite element code was validated by previously reported works for SMA structures using some case studies like uniaxial tension, bending of beams and deflection analysis of cylindrical panels (Mirzaeifar et al., 2009). In modeling torsion problems, quadratic axisymmetric elements with additional twist degree of freedom are used.[4]

As the thickness of the tube is very small[5] the radial change of martensitic volume fraction and stress is negligi-

---

[3] In 1540, Lodovico Ferrari found the solution of quartic equation by reducing it to a cubic equation. However, because the solution for cubic equations was not available at the time, his solution was not published. Four years later Ferrari's teacher, Gerolamo Cardano, published the solution of both quartic and cubic equations in his book *Ars Magna* (Cardano et al., 2007).

[4] Element CGAX8 in ABAQUS.

[5] In the finite element model, a tube with inner and outer radii, $r_i = 2.9$ mm and $r_o = 3.1$ mm is modeled.

Table 1
SMA material parameters.

Material constants	A generic SMA (Material I) (Qidwai and Lagoudas, 2000)	Ni$_{50}$Ti$_{50}$ (Material II) (Qidwai and Lagoudas, 2000; Jacobus et al., 1996)
E^A (Pa)	70.0×10^9	72.0×10^9
E^M (Pa)	30.0×10^9	30.0×10^9
$v^A = v^M$	0.3	0.42
α^A	22.0×10^{-6}/K	–
α^M	10.0×10^{-6}/K	–
$\rho\Delta c = c^M - c^A$ (J/(m^{3}K))	0.0	0.0
H	0.05	0.05
$\rho\Delta s_0$ (J/(m^{3}K))	-0.35×10^6	-0.42×10^6
A_f (K)	315.0	281.6
A_s (K)	295.0	272.7
M_s (K)	291.0	254.9
M_f (K)	271.0	238.8

ble. As a result, only one element is used in the radial direction. Although the stress distribution is constant along the axial direction, for avoiding high aspect ratio in the elements, 40 elements are used in the axial direction. The torsional loading is divided into 200 steps and the tolerance of 1×10^{-6} is considered for the convergence of transformation function (see Qidwai and Lagoudas, 2000).

Fig. 1 compares the results of the present formulation with those of the finite element simulations. Note that in the finite element results, the average stress value in the middle of thickness is shown. As it is seen, the numerical simulation predicts the completion of phase transformation in a larger twist angle compared to the exact solution. This difference can be reduced by increasing the number of finite elements, load steps, and iterations for achieving the equilibrium in the finite element simulation. It is worth mentioning that the results of the present closed-form solution are obtained without a massive computation in contrast with the finite element (or other numerical simulations) that require a massive iterative computational process. In the present case study, due to the small thickness of the tube, only one element through the thickness and a small number of elements (even one element) along
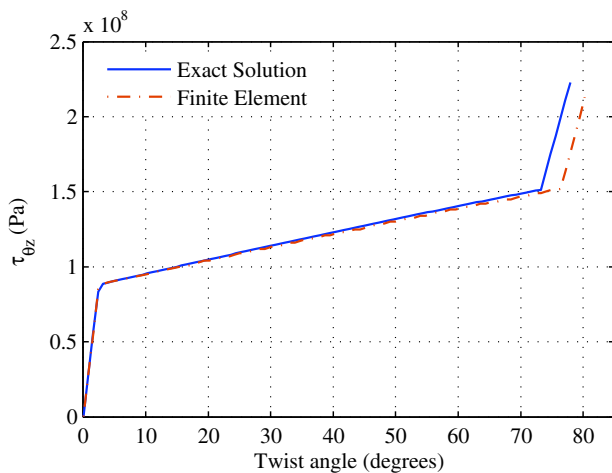
the length is adequate. However, in more complicated problems such as solid bars, with the increase of the element numbers in the model, the problem becomes challenging from the computational point of view and the present analytical solution would be much more efficient.

4.2. SMA solid bars

In this section, the loading and unloading of SMA solid prismatic bars with circular cross sections is considered. All the cases are presented for a bar with radius $R = 25$ mm with different material properties and different temperatures. In the first case we consider the loading of a bar, which is in the fully austenite phase at rest. In torsion of such a bar, in general, a cross section may be divided into three regions as shown in Fig. 2. In the inner region (Region I), the material is in the austenite phase and the relation $\tau_{\theta z} = G_A r \theta$ with $G_A = \frac{E_A}{2(1+v)}$ is valid. In Region II, the phase transformation has started ($0 < \xi < 1$) and the relation $\tau_{\theta z} = \wp^+(r,\theta)$ expressed in (22) is valid. In the outer region (Region III) the phase transformation is completed and the material is in the martensite phase. In this region stress is calculated as $\tau_{\theta z} = \tau_{\theta z}^f + G_M r(\theta - \theta^f)$, where $\tau_{\theta z}^f$ and θ^f are the shear stress and the twist angle at which the phase transformation is completed ($\xi = 1$). For a bar in the austenite phase with $\theta = 0$, increasing the twist angle the phase transformation starts from the outer radius and spreads toward the center. With more increase of the twist angle, the third region with fully transformed martensite spreads from the outer radius toward the center. For any value of the twist angle, as the material response in the austenite core is elastic, r_1 can be calculated by setting $\xi = 0$ in (15)$_1$ and replacing $\tau_{\theta z}$ with $G_A r \theta$. The radius of the inner elastic region r is calculated as:

$$r_1 = -\frac{1}{4}\frac{\sqrt{3}H - \sqrt{3H^2 - 8\Delta S_{44}f^+(T)}}{\Delta S_{44}G_A\theta}. \tag{23}$$

This equation can also be used for calculating the value of twist angle required for the start of phase transformation, which will obviously happen in the outermost layer $r = R$.

Consider an SMA solid bar with radius $R = 25$ mm and the material properties (Material I) in Table 1. All the
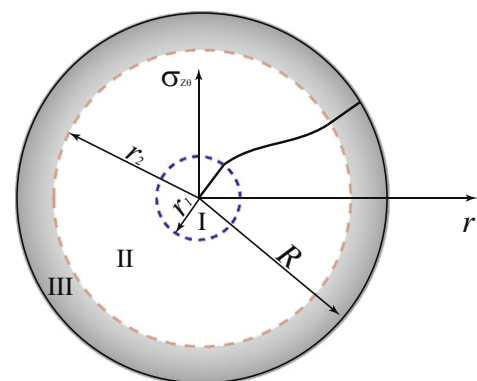

Fig. 1. Torsion of a SMA thin-walled tube in loading.

Fig. 2. Schematic of stress distribution in a circular bar. Regions I, II, and III are the austenite core, transition region, and the martensite outer layer, respectively.
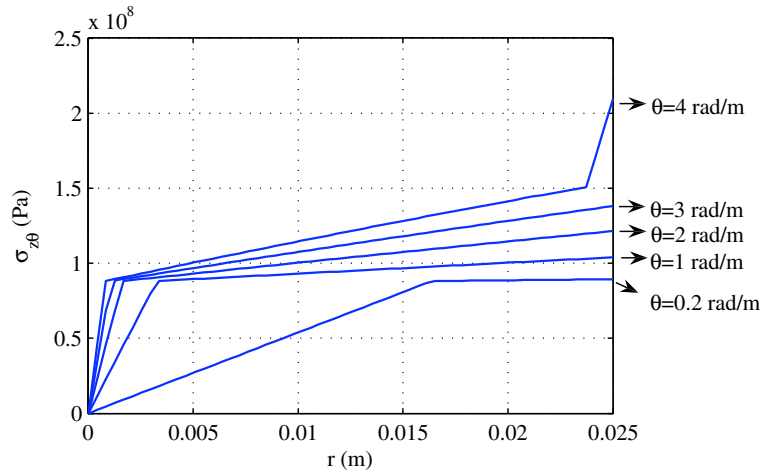
Fig. 3. Shear stress for various twist angels in loading.
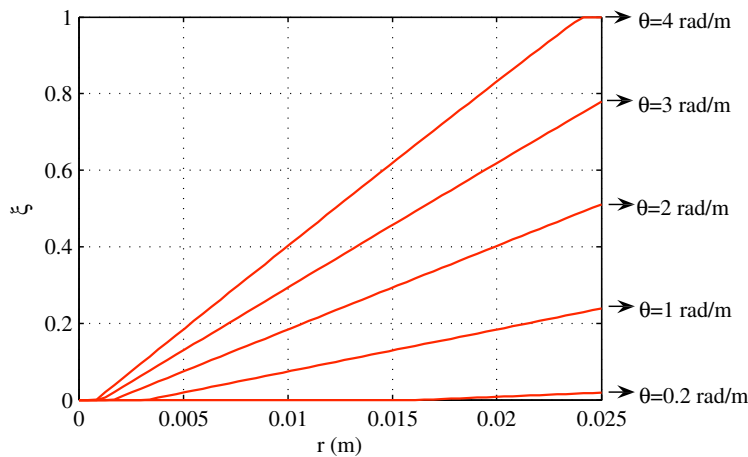

Fig. 4. Martensitic volume fraction for various twist angels in loading.

results are presented for different twist angles per unit length. Temperature is assumed to be T = 315 K. The shear stress distribution for various twist angels is shown in Fig. 3. Distribution of the martensitic volume fraction for these twist angles is depicted in Fig. 4.

As it is shown in Figs. 3 and 4 for the twist angle θ = 4 rad/m, the cross section is divided into three regions. For the inner region with 0 < r < 0.84 mm, the material is in the austenite phase. The annulus 0.84 mm < r < 23.7 mm is the phase transformation region and for r > 23.7 mm the phase transformation is completed and the material is in the martensite phase.

In the unloading of the SMA bar, all the points inside the elastic region will unload elastically in the stress–strain space with the rate of G_A ($\Delta\tau_{\theta z} = G_A r \Delta\theta$). For any point outside the elastic core with a martensitic volume fraction of 0 < ξ^* ⩽ 1 an elastic unloading with the rate of G_{eff} = $G_A + \xi(G_M - G_A)$ occurs until the stress level at the point reaches the value of [6]:

---

[6] This stress level is calculated by replacing ξ^- with ξ^* in (15)$_2$ and solving for $\tau_{\theta z}$.

$$\tau_{\theta z} = -\frac{1}{4} \frac{\sqrt{3}H - \sqrt{3H^2 - 8\Delta S_{44}f^-(T) + 8\Delta S_{44}\xi^*\rho b^A}}{\Delta S_{44}}. \quad (24)$$

After reaching this stress, the stress–strain relation $\tau_{\theta z} = \wp^-(r,\theta)$ for unloading expressed in (22) will determine the shear stress for any twist angle. The cross section will be divided into three regions in unloading: the austenite core with elastic unloading, the transition region with 0 < ξ ⩽ 1, which has inelastic loading but elastic loading, and the outer region with inelastic loading and unloading. It is clear that in some special unloaded twist angles the third region does not exist. As another case study, the bar of the previous example loaded to θ = 4 rad/m is unloaded to different twist angles. The stress distribution for the unloading is shown in Fig. 5. The martensitic volume fraction distribution corresponding to these twist angles are shown in Fig. 6.

As it is shown in Figs. 5 and 6, in the unloading up to θ = 3.8 rad/m all the points in the cross section have an elastic unloading and phase transformation does not start during unloading (the martensitic volume fraction does not change). However, for larger values of unloading twist,
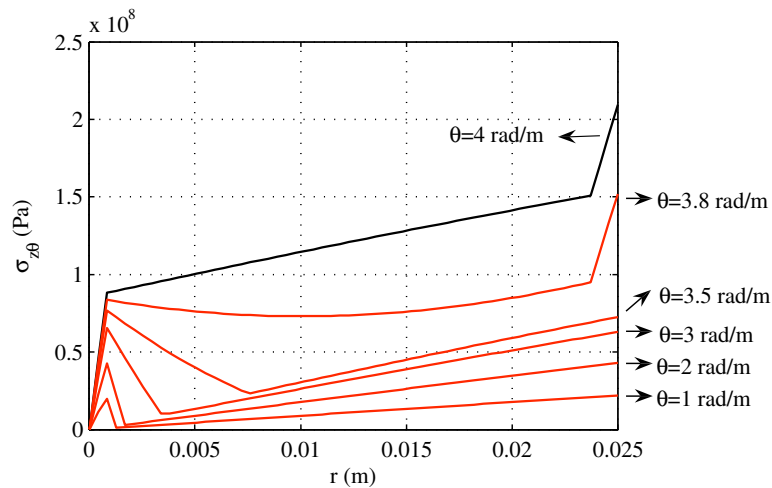
Fig. 5. Shear stress for various twist angels in unloading.

all the three regions can be distinguished. It is obvious that stress and martensitic volume fraction distributions in this case are history dependent and are not identical in loading and unloading for the same values of twist angle (compare Figs. 5 and 6 with Figs. 3 and 4). Note that, at the present temperature ($T = A_f = 315$ K) all the loading induced stresses recover during a complete unloading.

In the next case study, the effect of temperature on the response of the bar is studied. Shear stress distribution for the twist angle of $\theta = 3.8$ rad/m is depicted in Fig. 7 for three different temperatures. It is seen that increasing temperature, the stress corresponding to the onset of phase transformation increases and consequently the radius of the elastic core increases as well. Also, for lower temperatures Region III starts to spread toward the center for lower values of twist angle per unit length.

Next we study the effect of material properties on the response of circular bars in torsion. Two identical bars with material constants I and II are considered. Both bars are initially in the austenite finish temperature ($T = 315$ K for Material I and $T = 281.6$ K for Material II). As it is shown in Fig. 8, in loading for Material II the phase transformation

starts at a higher stress level and the radius of the elastic core is larger. In unloading, the bar made of Material II has a lower stress level in the region with reverse phase transformation. As it will be shown shortly, the difference between shear stress distribution for these two materials will significantly affect the torque applied to the bar in loading and unloading. It is worth noting that, as the elastic properties of these two materials are almost the same, the difference in material response is mainly caused by the difference in the parameters $f^\pm(T)$.

All the previous case studies were presented for different twist angles. In some cases, it is necessary to calculate the response of the bar with respect to the applied torque. For this purpose the present formulation can be used for calculating the necessary torque for producing a specific twist angle as:

$$T^+ = 2\pi \int_0^{r_1} G_A \theta r^3 dr + 2\pi \int_{r_1}^{r_2} \wp^+(r, \theta) r^2 dr$$
$$+ 2\pi \int_{r_2}^{R} \left(\tau_{\theta z}^f + G_M r(\theta - \theta^f) \right) r^2 dr, \quad (25)$$
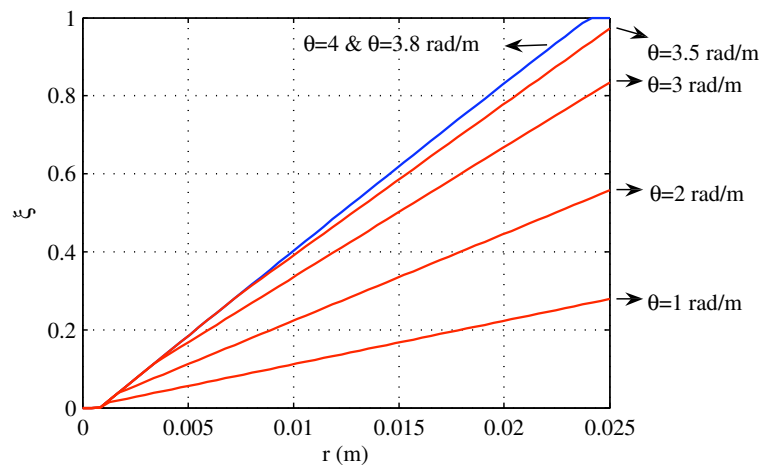

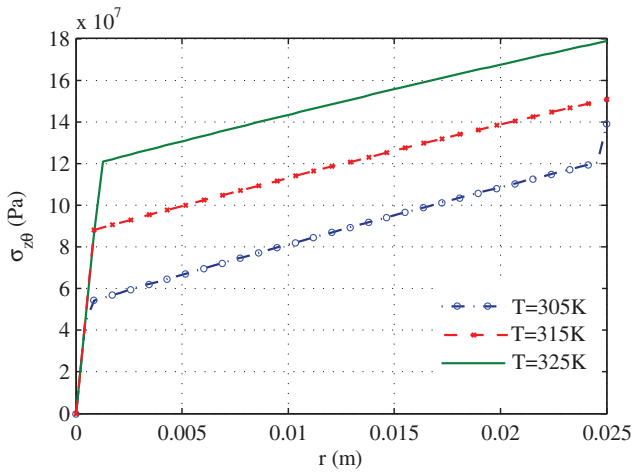**Fig. 6.** Martensitic volume fraction for various twist angels in unloading.

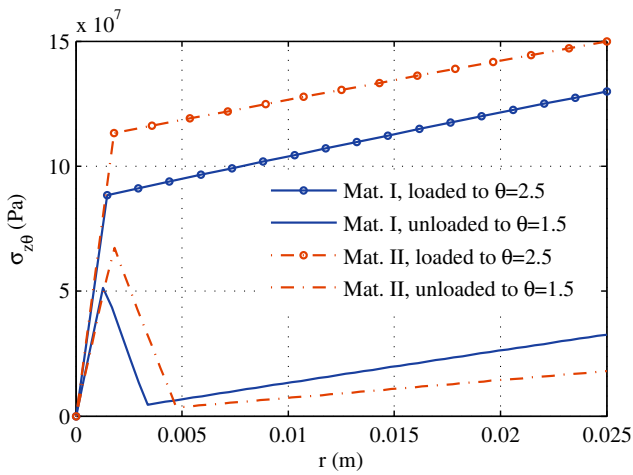**Fig. 7.** Shear stress distribution for three different temperatures.

Fig. 8. Shear stress for two different material properties in loading and unloading.

$$T^- = 2\pi \int_0^{r_1^*} G_A \theta r^3 dr + 2\pi \int_{r_1^*}^{r_2^*} (\tau_{\theta z}^\ell - G_{eff} r \Delta\theta) r^2 dr$$

$$+ 2\pi \int_{r_2^*}^{R} \wp^-(r, \theta) r^2 dr, \qquad (26)$$

where r_1 and r_2 are the inner and outer radii of Regions II as shown in Fig. 2 in loading. The parameters r_1^* and r_2^* are the inner and outer radii of Region II with phase transformation during the loading phase but in an elastic unloading. The parameter $\tau_{\theta z}^\ell$ represents the value of shear stress for any point at the end of the loading phase and $\Delta\theta$ is the amount of reverse twist angle during unloading. The loading–unloading cycle for a bar with the same geometry as those of the previous examples is depicted in Fig. 9 for three different temperatures. Material I is used for this case study. As it is shown in this figure, the twist angle is fully recovered during unloading for temperatures above the austente finish temperature and after removing the applied torque no residual twist is remained in the bar. For $T = 305$ K, which is below the austenite finish temperature, when the applied torque is removed, a residual twist is ob-
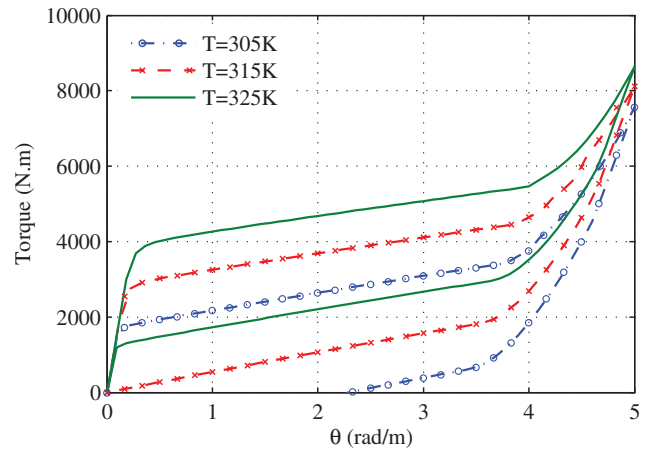

Fig. 9. Torque versus twist angle in a loading–unloading cycle for Material I at different temperatures.

served. In all the three temperatures, the area of the hysteresis loop remains constant; the loops are rigidly translated in the torque-twist plane.

As shown in Fig. 9, for temperatures below the austenite finish temperature a residual twist angle and consequently a residual stress distribution exists after removing the applied torque. As another case study, a bar at $T = 305$ K is loaded to different maximum twist angles and the applied torque is removed to study the residual twist and stress distributions. Fig. 10 shows the applied torque versus twist angle for this bar. As it is shown, for a bar loaded to $\theta = 4$ and 6 rad/m after removing the torque, the bar has a residual twist angle of $\theta = 2.31$ rad/m. In the case of loading the bar to $\theta = 2$ rad/m, after removing the external torque, the residual twist angle is $\theta = 1.78$ rad/m. Distribution of residual shear stress for these bars is shown in Fig. 11. As it is shown, removing the external torque the bar is in a state of self-equilibrated residual stress distribution.

The loading–unloading hysteresis loop in torsion for different material properties is studied in the next case study. Fig. 12 shows the applied torque versus the twist angle for a bar of the previous examples made of Materials I and II
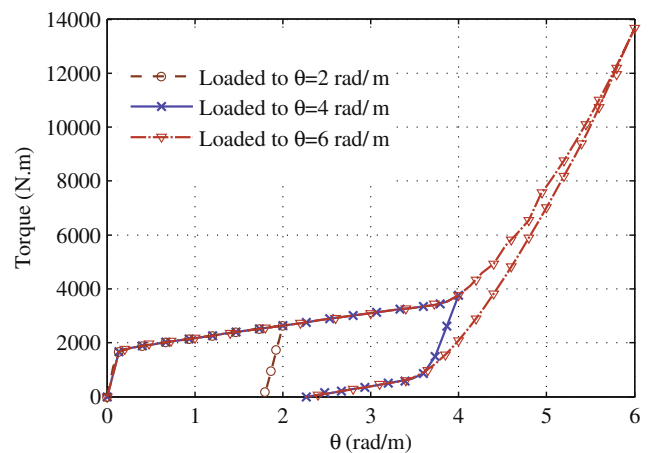

Fig. 10. Torque versus twist angle for $T = 305$ K at different maximum loading twist angles.
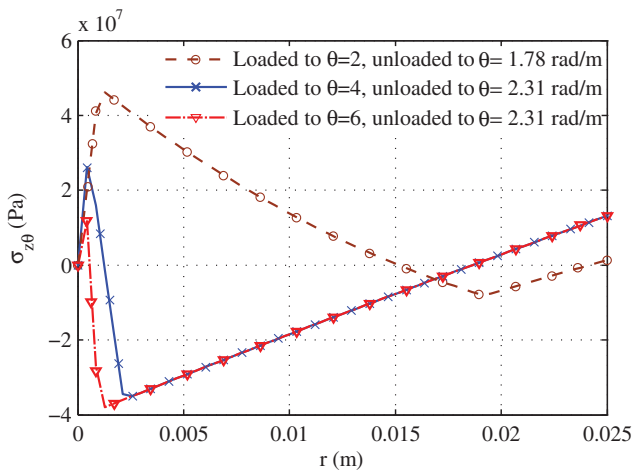
Fig. 11. Residual stress distribution for T = 305 K for identical bars loaded to different maximum twist angles.
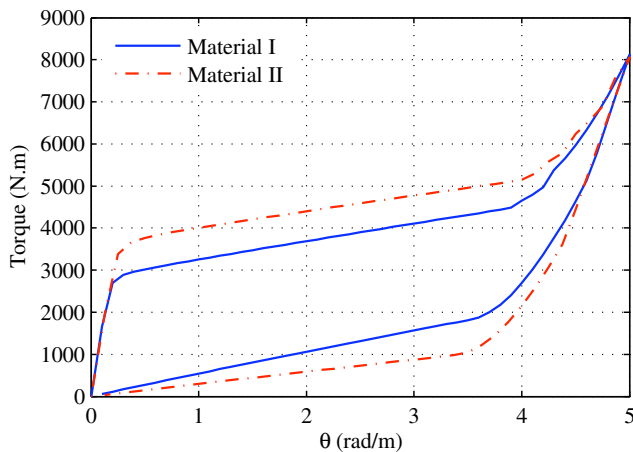

Fig. 12. Torque versus twist angle in loading–unloading cycle for two different material properties.

(both bars are in the austenite finish temperature). As it is shown in this figure, the hysteresis loop area is larger for Material II. This can be explained by looking at the stress distribution shown in Fig. 8. For Material II, the phase transformation starts at a higher stress level in loading and the reverse phase transformation occurs at lower stress levels in unloading.

5. Conclusions

In this paper, an analytical solution is presented for the pure torsion of SMA bars with circular cross sections. We reduced a general phenomenological macroscopic constitutive model for polycrystalline SMAs and obtained an explicit expression for the shear stress in circular SMAs bars in pure torsion. It is shown that in the most general case, the cross section in loading and unloading may be divided into three regions with different responses. The stress–strain relation in these regions is derived and the shear stress distribution is calculated for different twist angles both in loading and unloading. Several case studies are presented for analyzing the response of SMA bars with different material properties at various temperatures. The twist angle is obtained as a function of the applied torque in loading–unloading cycles. The presented solution can be used as a benchmark problem for validating numerical simulations of SMAs. This method can also be exploited to analyze SMA helical springs, which have various applications in engineering. This will be the subject of a future communication.

Appendix A. Analytical expressions for shear stress in loading and unloading

In this appendix, the explicit expression for the shear stress is given. Using the constants in (21), the following parameters are introduced:

$$G_1 = -\frac{3}{8}(F_1)^2 + F_2, \quad G_1^* = F_2^*, \quad G_2 = \frac{1}{8}(F_1)^3 - \frac{1}{2}F_1F_2 + F_3,$$

$$G_2^* = -\frac{1}{2}F_1F_2^* + F_3^*,$$

$$G_3 = -\frac{3}{256}(F_1)^4 + \frac{1}{16}(F_1)^2F_2 - \frac{1}{4}F_1F_3 + F_4,$$

$$G_3^1 = \frac{1}{16}(F_1)^2F_2^* - \frac{1}{4}F_1F_3^* + F_4^*,$$

$$K_1 = -\frac{1}{12}(G_1)^2 - G_3, K_1^* = -\frac{1}{6}G_1G_1^* - G_3^1,$$

$$K_1^\diamond = -\frac{1}{12}(G_1^*)^2,$$

$$K_2 = -\frac{1}{108}(G_1)^3 + \frac{1}{3}G_1G_3 - \frac{1}{8}(G_2)^2,$$

$$K_2^* = -\frac{1}{36}(G_1)^2G_1^* + \frac{1}{3}G_1G_3^* + \frac{1}{3}G_3G_1^* - \frac{1}{4}G_2G_2^*,$$

$$K_2^\diamond = -\frac{1}{36}G_1G_1^* + \frac{1}{3}G_1^*G_3 - \frac{1}{8}(G_2^*)^2, \quad K_2^\circ = -\frac{1}{108}(G_1^*)^3,$$

$$\text{(A.1)}$$

and,

$$\mathcal{R} = -\frac{1}{2}K_2 - \frac{1}{2}K_2^* r\theta - \frac{1}{2}K_2^\diamond r^2\theta^2 - \frac{1}{2}K_2^\circ r^3\theta^3$$
$$+ \left[\frac{1}{4}(K_2)^2 + \frac{1}{2}K_2K_2^* r\theta + \frac{1}{2}K_2K_2^\diamond r^2\theta^2 + \frac{1}{2}K_2K_2^\circ r^3\theta^3 + \frac{1}{4}(K_2^*)^2 r^2\theta^2\right.$$
$$+ \frac{1}{2}K_2^* r^3\theta^3 K_2^\diamond + \frac{1}{2}K_2^*K_2^\circ r^4\theta^4 + \frac{1}{4}\left(K_2^\diamond\right)^2 r^4\theta^4 + \frac{1}{2}K_2^\diamond K_2^\circ r^5\theta^5$$
$$+ \frac{1}{4}(K_2^\circ)^2 r^6\theta^6 + \frac{1}{27}(K_1)^3 + \frac{1}{9}(K_1)^2 K_1^* r\theta + \frac{1}{9}(K_1)^2 K_1^\diamond r^2\theta^2$$
$$+ \frac{1}{9}K_1(K_1^*)^2 r^2\theta^2 + \frac{2}{9}K_1K_1^*K_1^\diamond r^3\theta^3$$
$$+ \frac{1}{9}K_1\left(K_1^\diamond\right)^2 r^4\theta^4 + \frac{1}{27}(K_1^*)^3 r^3\theta^3 + \frac{1}{9}(K_1^*)^2 K_1^\diamond r^4\theta^4$$
$$\left. + \frac{1}{9}K_1^*\left(K_1^\diamond\right)^2 r^5\theta^5 + \frac{1}{27}(K_1^\diamond)^3 r^6\theta^6\right]^{\frac{1}{2}},$$

$$\mathcal{U} = (\mathcal{R})^{\frac{1}{3}}, \quad \mathcal{Q} = K_2 + K_2^* r\theta + K_2^\diamond r^2\theta^2 + K_2^\circ r^3\theta^3,$$

$$\alpha = G_1 + G_1^* r\theta, \beta = G_2 + G_2^* r\theta,$$

$$\mathcal{P} = K_1 + K_1^* r\theta + K_1^\diamond r^2\theta^2, \quad \mathcal{Y} = -\frac{5}{6}\alpha + \mathcal{U} - \frac{1}{3}\frac{\mathcal{P}}{\mathcal{U}},$$

$$\mathcal{W} = \sqrt{\alpha + 2\mathcal{Y}}. \quad \text{(A.2)}$$

The quartic Eq. (20) has four roots. Among these, only one satisfies the continuity condition for the shear stress distri-

bution at R_1 (see (23)). This admissible solution is expressed as:

$$\tau_{\theta z} = \wp^{\pm}(r, \theta)$$
$$= -\frac{1}{4}F_1 + \frac{1}{2}\mathcal{W} - \frac{1}{2}\sqrt{-3\alpha - 2\mathcal{Y} - 2\frac{\beta}{\mathcal{W}}}, \qquad (A.3)$$

where $\wp^+$ and $\wp^-$ are solutions for loading and unloading, respectively. In loading, $\wp^+(r, \theta)$ is calculated by considering the parameters with (+) sign in (21) and in unloading $\wp^-(r, \theta)$ is calculated by considering the parameters with (−) sign in (21).

References

Ancker, C.J., Goodier, J.N., 1958a. Pitch and curvature corrections for helical springs. Transactions of the ASME – Journal of Applied Mechanics 25, 466–470.

Ancker, C.J., Goodier, J.N., 1958b. Theory of pitch and curvature corrections for the helical springs – I (tension). Transactions of the ASME – Journal of Applied Mechanics 25, 471–483.

Ancker, C.J., Goodier, J.N., 1958c. Theory of pitch and curvature corrections for the helical springs – II (torsion). Transactions of the ASME – Journal of Applied Mechanics 25, 484–495.

Andrawes, B., DesRoches, R., 2007. Comparison between shape memory alloy seismic restrainers and other bridge retrofit devices. Journal of Bridge Engineering 12 (6), 700–709.

Andrawes, B., DesRoches, R., 2008. Sensitivity of seismic applications to different shape memory alloy models. Journal of Engineering Mechanics 134 (2), 173–183.

Bo, Z., Lagoudas, D.C., 1999. Thermomechanical modeling of polycrystalline SMAs under cyclic loading Part I: Theoretical derivations. International Journal of Engineering Science 37, 1089–1140.

Boyd, J.G., Lagoudas, D.C., 1996. A thermodynamic constitutive model for the shape memory alloy materials. Part I. The monolithic shape memory alloy. International Journal of Plasticity 12, 805–842.

Brinson, L.C., 1993. One-dimensional constitutive behavior of shape memory alloy: thermomechanical derivation with non-constant material functions and redefined martensite internal variable. Journal of Intelligent Material Systems and Structures 4, 229–242.

Cardano, G., Witmer, T.R., Ore, O., 2007. The Rules of Algebra: (ars Magna). Dover Publications.

Chen, T., 2004. A homogeneous elliptical shaft may not warp under torsion. Acta Mechanica 169, 221–224.

Chung, J.H., Heo, J.S., Lee, J.J., 2006. Modeling and numerical simulation of the pseudoelastic behavior of shape memory alloy circular rods under tension?torsion combined loading. Smart Materials and Structures 15, 1651–1660.

Coulomb, C.A., 1784. Recherches théoriques et expérimentales sur la force de torsion, et sur l'élasticité des fils de métal. Mémoires de l'Académie Royale des Sciences, pp. 229–269.

DesRoches, R., Smith, B., 2004. Shape memory alloys in seismic resistant design and retrofit: a critical review of their potential and limitations. Journal of Earthquake Engineering 8, 415–429.

Dong, Y., Boming, Z., Jun, L., 2008. A changeable aerofoil actuated by shape memory alloy springs. Materials Science and Engineering A 485, 243–250.

Higgins, T.J., 1942. A comprehensive review of Saint–Venant's torsion problem. American Journal of Physics 10 (5), 248–259.

Jacobus, K., Sehitoglu, H., Balzer, M., 1996. Effect of stress state on the stress-induced martensitic transformation in polycrystalline Ni–Ti alloy. Metallurgical and Materials Transactions A 27, 3066–3073.

Leea, C.Y., Zhuob, H.C., Hsu, C.W., 2009. Lateral vibration of a composite stepped beam consisted of SMA helical spring based on equivalent Euler–Bernoulli beam theory. Journal of Sound and Vibration 324, 179–193.

Liew, K.M., Kitipornchai, S., Ng, T.Y., Zou, G.P., 2002. Multi-dimensional superelastic behavior of shape memory alloys via nonlinear finite element method. Engineering Structures 24, 51–57.

Lim, T.J., McDowell, D.L., 1999. Mechanical behavior of an Ni–Ti shape memory alloy under axial-torsional proportional and nonproportional loading. Transactions of the ASME – Journal of Engineering Materials and Technology 121, 9–18.

Mahapatra, D.R., Melnik, R.V.N., 2007. Finite element approach to modelling evolution of 3D shape memory materials. Mathematics and Computers in Simulation 76, 141–148.

Mirzaeifar, R., 2009. A new method for analyzing thick walled shape memory alloy cylinders subjected to internal pressure. In: ASME Conference on Smart Materials, Adaptive Structures and Intelligent Systems (SMASIS), September 21–23, Oxnard, California USA.

Mirzaeifar, R., Shakeri, M., Sadighi, M., 2009. Nonlinear finite element formulation for analyzing shape memory alloy cylindrical panels. Smart Materials and Structures 18 (3), 035002.

Qidwai, M.A., Lagoudas, D.C., 2000. Numerical implementation of a shape memory alloy thermomechanical constitutive model using return mapping algorithms. International Journal for Numerical Methods in Engineering 47, 1123–1168.

Qidwai, M.A., Lagoudas, D.C., 2000. On thermomechanics and transformation surfaces of polycrystalline NiTi shape memory alloy material. International Journal of Plasticity 16, 1309–1343.

Sokolnikoff, I.S., 1956. Mathematical Theory of Elasticity. McGraw-Hill, New York.

Speicher, M., Hodgson, D.E., DesRoches, R., Leon, R.T., 2009. Shape memory alloy tension/compression device for seismic retrofit of buildings. Journal of Materials Engineering and Performance 18, 746–753.

Tanaka, K., 1986. A thermomechanical sketch of shape memory effect: one-dimensional tensile behavior. RES Mechanica 18 (3), 251–263.

Tobushi, H., Tanaka, K., 1991. Deformation of a shape memory alloy helical spring: analysis based on stress–strain–temperature relation. JSME International Journal, Series I 34, 83–89.

Toi, Y., Lee, J.B., Taya, M., 2004. Finite element analysis of superelastic, large deformation behavior of shape memory alloy helical springs. Computers and Structures 82, 1685–1693.

Wahl, A.M., 1944. Mechanical Springs. Penton Publishing Company, Cleveland, USA.